International Journal of Coal Science & Technology (2023) 10:35
https://doi.org/10.1007/s40789-023-00590-9

RESEARCH

Study of energy-efficient heat resistance and cooling technology for high temperature working face with multiple heat sources in deep mine

Hongbin Zhao[1] · Shihao Tu[1] · Xun Liu[1] · Jieyang Ma[1] · Long Tang[1]

Received: 30 May 2022 / Revised: 20 August 2022 / Accepted: 4 May 2023

Abstract
In the present research, we proposed a scheme to address the issues of severe heat damage, high energy consumption, low cooling system efficiency, and wastage of cold capacity in mines. To elucidate the seasonal variations of environmental temperature through field measurements, we selected a high-temperature working face in a deep mine as our engineering background. To enhance the heat damage control cability of the working face and minimize unnecessary cooling capacity loss, we introduced the multi-dimensional heat hazard prevention and control method called "Heat source barrier and cooling equipment". First, we utilize shotcrete and liquid nitrogen injection to eliminate the heat source and implemented pressure equalization ventilation to disrupt the heat transfer path, thereby creating a heat barrier. Second, we establish divisional prediction models for airflow temperature based on the variation patterns obtained through numerical simulation. Third, we devise the location and dynamic control strategy for the cooling equipment based on the prediction models. The results of field application show that the heat resistance and cooling linkage method comply with the safety requirement throughout the entire mining cycle while effectively reducing energy consumption. The ambient temperature is maintained below 30 °C, resulting in the energy saving of 10% during the high-temperature period and over 50% during the low-temperature period. These findings serve as a valuable reference for managing heat damage in high-temperature working faces.

Keywords High-temperature working face · Heat source barrier · Multiple heat source effect · Airflow temperature prediction · Dynamic control strategy

1 Introduction

In the last years, industrial and mining technologies have rapidly evolved. Unfortunately, shallow recoverable coal resources have gradually decreased as depth of mining has increased in addition to severe underground thermal pollution (Yao 2018). Working faces in deep mines are always characterized by high temperatures of the surrounding rocks, complex and regional concentration of heat sources, and goaf heat intrusion, among others (Liu et al. 2018; Jayasuriya et al. 2022), which result in the emergence of areas with severe underground heat damage. In order to ensure the safety of workers and production efficiency, heat harm is controlled by applying different measures.

At present, heat damage in high-temperature coal faces is prevented by using different strategies including heat barrier and mechanical refrigeration. Zou et al. (2016) used heat insulation shunt cooling to change the heat transfer and airflow structure of roadways, and reduced the airflow temperature on the working face. Chang et al. (2021) proposed a cool-wall cooling system, where they placed a heat absorption plate on the roadway wall to absorb and isolate the heat dissipation from the surrounding rock. With this, wind temperature in the roadway was reduced by 3 °C. Liu and Zhang (2017) developed a bubble composite heat insulation system with expanded perlite as the main material, which reduced the heat dissipation of the roadway surrounding rock. In this case, the temperature of the roadway airflow outlet decreased by 4.956 °C. In addition to blocking the heat dissipation of roadway surrounding rock, the blocking of goaf heat source is also an important mean to control the

✉ Shihao Tu
tsh@cumt.edu.cn

[1] Key Laboratory of Deep Coal Resource Mining (Ministry of Education of China), School of Mines, China University of Mining and Technology, Xuzhou 221116, China

thermal damage of the working face (Wang et al. 2020). Xue et al. (2020) applied a microcapsule foam gel barrier to the goaf, which prevented the spontaneous combustion of the coal left in the goaf and successfully isolated the goaf heat. Akira Yoshida et al. (2015) determined that inert gas-retarded water mist quickly suppressed spontaneous coal combustion. This was successfully applied for fire prevention in coal mine goaf. These heat source barrier methods display good performance; however, the heat barrier effect gradually declines with time. In addition, the barrier cannot meet the cooling demands of ultra-high-temperatures of the working face found in deep levels of mines. In order to solve these problems, many scholars (Zhang et al. 2020; Zhai et al. 2019; Buys et al. 2015) have proposed the use of mechanical refrigeration and other cooling equipment. Brake and Fulker (2000), in collaboration with Mount Isa Mines, developed a comprehensive cooling system and supporting solution to deal with the high temperature thermal damage of deep well mining. For this purpose, they measured and calculated different thermal parameters for the optimization of the ventilation and bulk air-cooling systems. Steven Bluhm et al. (2014) established a complete mine cooling system for Resolution Copper Mine and introduced the main components of the ground and underground cooling systems, such as central surface cooling machines, surface bulk air coolers, and centralized underground cooling machines, among others. The double cooling scheme reduced the threat of heat damage. Stephen G Hardcastle (2004) was able to regulate the underground climate by optimizing the ventilation system. Herein, local cooling measures were implemented according to actual cooling requirements of operations personnel and machines by establishing local microclimate environments to ensure safe operations. Kuyuk et al. (2019) designed a deep mine cooling system based on natural lakes, making full use of low temperature lake water for cooling. Guo et al. (2017) created the HEMS cooling system, which uses underground cold water to absorb heat. With this method, the cooling of high-temperature working faces was performed by taking advantage of geothermal resources. Du Plessis et al. (2013) proposed a flow-changing energy-saving strategy based on the original mine integrated cooling system, which reduces energy consumption as long as cold is supplied. However, these schemes present several problems including complex system composition, low DOF (degree of freedom) of regulation, and severe cold waste. Because of this, the cooling equipment cannot be moved according to seasonal variations and the cold requirements. Therefore, it is necessary to adopt a new energy-saving and efficient cooling scheme.

According to this analysis and considering the disadvantages of the existing techniques for working face cooling, in the present research we considered both aspects, the heat source barrier and cooling equipment. First, we propose to use heat source barrier methods for the two main heat sources located in the surrounding rock and goaf of the high-temperature working face. In addition, the layout scheme and intelligent control strategy of the cooling equipment was considered. Finally, we selected the 74104 high-temperature working face of a deep well as engineering background in order to analyze the potential practical application.

2 Project overview

In the present study, the 74104 high-temperature working face of a deep mining well in Jiangsu Province of China was selected as engineering background. The 74104 working face was located at a depth of 1150 m, which corresponds to deep mining conditions. The working face was mined along a strike length of 1374 m and an inclined length of 175 m. The minable coal seam corresponded to the No. 7 coal seam, with an average thickness of 3.18 m, and average dip angle of 23°.The coal seam where the 74104 working face was located had a spontaneous ignition grade of Class I, which indicated that coal seam was prone to spontaneous combustion. The mining of the 74104 working face began on Jun 1st, 2020, with a daily advance speed of 3 m/d and air volume ventilation of 1400 m^3/min. The original rock temperature reached 42 °C, indicating a second-degree heat hazard level.

In order to reflect the change rule of airflow temperature more directly and formulate an optimal cooling scheme for high-temperature working faces, temperature and humidity sensors were used for field measurement. These measurements were performed in seven different points of the hydraulic supports located in the working face (nearly 10 m one from the other) and at intervals of 200 m in headentry and tailentry. In addition, measurements were performed at the inlet and outlet of airflow in each region. Six representative measurement points on the ventilation route of the 74104 working face were calibrated. Point 1 was located in front of the cooling fan in the subinclined shaft; point 2 was located at the inlet of the 74104 headentry; point 3 was located at the 500 m milestone of the 74104 headentry; point 4 was located at the inlet of the 74104 working face; point 5 was located at the center of the 74104 working face; and point 6 was located at the outlet of the 74104 working face. Measurement points are shown in Fig. 1.

Mining of the 74104 working face began on June 1st, 2020. In addition, the airflow temperature measurements were performed every seven days starting June 2nd. Temperatures were taken between 12:00 p.m. and 14:00 p.m., where the highest temperatures occur.

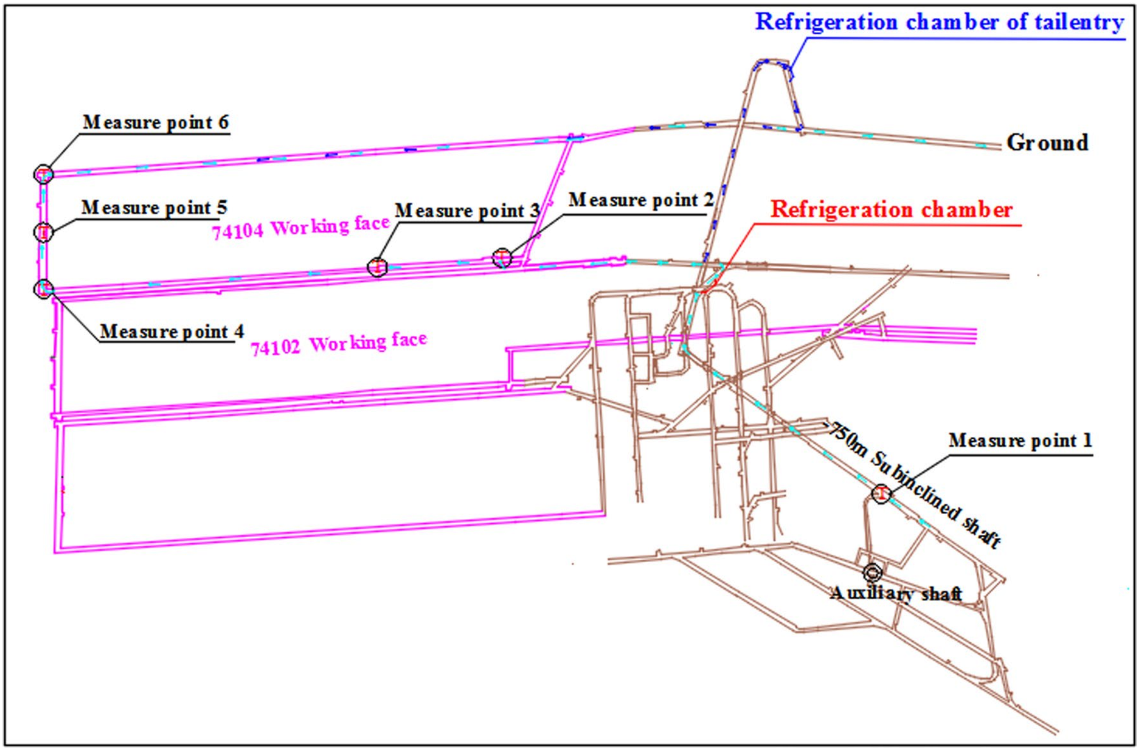

Fig. 1 Location of the points where meteorological parameters where measured

3 Heat barrier method

The first step considered the partial obstruction of the heat source in the high-temperature working face, which reduced both, heat dissipation and refrigerant pressure of the cooling equipment. The heat barrier scheme considered the heat dissipation of surrounding rock and goaf. For this purpose, shotcrete and water spray were used to reduce the heat dissipation of surrounding rock. In addition, a wall was used to obstruct the heat dissipation of transported coal and gangue (Wang and Zhou 2020). In order to eliminate heat source, spontaneous combustion of residual coal was hindered (Zhang et al. 2019). Also, in order to cut off heat transfer, air leakage was reduced.

Prior to the working face mining, the sampling beam tubes were placed at different intervals in the tailentry, these sampling beam tubes successively entered the goaf with the advance of the working face (Ray and Singh 2007). Later, the location of the "spontaneous combustion zone" can be identified by extracting and analyzing the gas in the beam tube to obtain the oxygen concentration in different areas. Finally, liquid nitrogen was injected into the "spontaneous combustion zone" and goaf heat was eliminated from the source.

The pressure equalization and ventilation technologies are used to decrease the rate of air leakage during the mining of the working face. However, this method results in the increase of air leakage into the goaf and spontaneous combustion of residual coal. In order to solve the contradiction between two key points, it is necessary to determine the optimal pressure difference ΔP and the position of pressure equalization point.

Because of the even-distributed characteristics of wind resistance, the air pressure decreases linearly in the working face (Tamminen et al. 2016). First, assuming the air pressure in the inlet side is P_a, the air pressure in the return side (upper corner) is P_b, and the air pressure inside the goaf maintains a stable value P_g. Then, the pressure equalization point is x_0, and P_0 equals to P_g at this point. In order to reach the optimal pressure difference ΔP and the position of the pressure equalization point, the upper corner of the working face is taken as the coordinate origin to establish a rectangular coordinate system. As seen in Fig. 2, the x-axis represents the length of any point from the upper corner, and the y-axis represents the amount of air leakage at any point. Moreover, P_g, P_a, and L values are known.

$$P_0 = P_a - \frac{\Delta P}{L}(L - x_0) = P_g \tag{1}$$

$$\frac{\Delta P}{L} = \frac{P_a - P_g}{L - x_0} \tag{2}$$

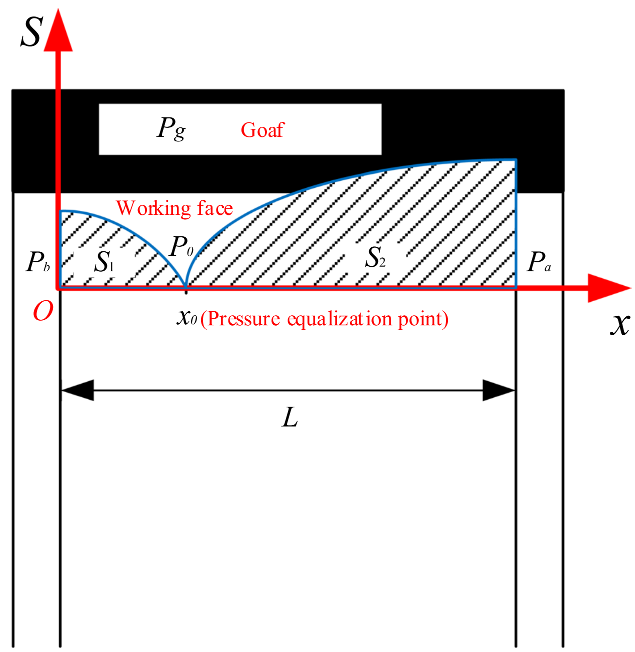

Fig. 2 Relationship between air leakage rate and relative position under pressure equalization ventilation

The differential pressure gap method was used to calculate the air leakage (Lolon et al. 2017; Wu et al. 2019).

$$S = 0.67 \times A \times \sqrt{\Delta P} \tag{3}$$

Here, S is the air leakage, A is the air leakage area, and ΔP is the differential pressure. Later, the Equation used to calculate the total air leakage caused by the pressure difference between goaf and working face can be obtained:

$$S = \int_0^{x_0} 0.67A\sqrt{P_g - \left[P_a - \frac{\Delta P}{L}(L-x)\right]}dx + \int_{x_0}^{L} 0.67A\sqrt{P_a - \frac{\Delta P}{L}(L-x) - P_g}dx \tag{4}$$

Equation (5) is obtained by incorporating Eq. (2) into Eq. (4) and making $m = \frac{P_a - P_g}{L - x_0}$.

$$S = 0.67A\int_0^{x_0}\sqrt{mx_0 - mx}dx + 0.67A\int_{x_0}^{L}\sqrt{mx - mx_0}dx \tag{5}$$

Solving the definite integral of the right-hand side of the equation and making $\sqrt{mx_0 - mx} = z$, $\sqrt{mx - mx_0} = t$.

$$S = 0.67A\int_{\sqrt{mx_0}}^{0} -\frac{2z^2}{m}dz + 0.67A\int_0^{\sqrt{mL - mx_0}} \frac{2t^2}{m}dt \tag{6}$$

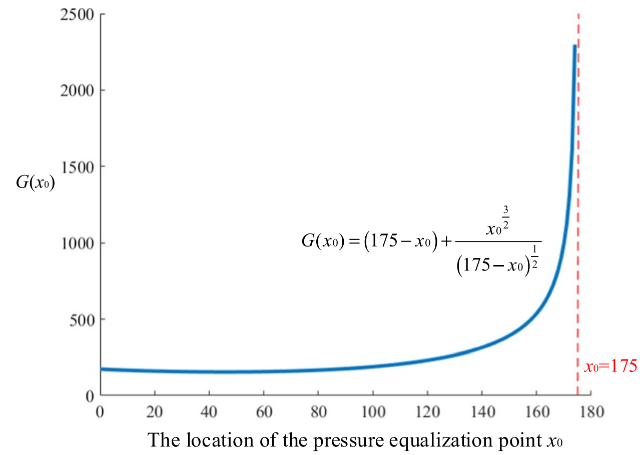

Fig. 3 Function $G(x_0)$

$$S = 0.67A\left[\frac{2\left(\sqrt{mL - mx_0}\right)^3}{3m} + \frac{2\left(\sqrt{mx_0}\right)^3}{3m}\right] \tag{7}$$

When m is introduced into Eq. (7), the final Eq. (8) can be obtained.

$$S = 0.447A \times \left(P_a - P_g\right)^{\frac{1}{2}}\left[\left(L - x_0\right) + \frac{x_0^{\frac{3}{2}}}{\left(L - x_0\right)^{\frac{1}{2}}}\right] \tag{8}$$

$$G(x_0) = \left(L - x_0\right) + \frac{x_0^{\frac{3}{2}}}{\left(L - x_0\right)^{\frac{1}{2}}} \tag{9}$$

Equation (8) can be decomposed in two parts, the first half is a constant and the second half is a function of x_0. Figure 3 represents the function $G(x_0)$ when L equals 175 m.

The minimum total air leakage of the working face can be obtained through derivation of the function $G(x_0)$ without considering actual engineering requirements.

$$G'(x_0) = 1.5x_0^{\frac{1}{2}}(175 - x_0)^{-\frac{1}{2}} + 0.5x_0^{\frac{3}{2}}(175 - x_0)^{-\frac{3}{2}} - 1 \tag{10}$$

The function $G(x_0)$ decreases monotonically when x_0 ranges from 0 to 45.657 m, but increases monotonically when x_0 ranges from 45.657 to 175 m. Therefore, the air leakage of the working face reaches the minimum $69.9475A \times \left(P_a - P_g\right)^{\frac{1}{2}}$ as the pressure equalization point is located 45.657 m from the upper corner. The pressure difference ΔP between the two ends of the working face is $1.353(P_a\text{-}P_g)$. In addition, the upper corner should be set as the pressure equalization point in order to improve the heat barrier effect. On the other hand, to ensure the best heat barrier effect while reducing spontaneous combustion of residual coal, the pressure equalization point should be moved away from the upper corner. Selection of the specific location of the pressure equalization point should be based on multiple factors including the advancing speed of working face, the speed of air leakage, spontaneous combustion period of coal seam, and gas emissions.

Considering this analysis, the pressure equalization ventilation system in high-temperature working face was designed and the specific layout is shown in Fig. 4.

First, it is necessary to determine the periodic variation of air pressure in the goaf or relatively stable P_g value. Next, the local fan model and reasonable working condition can be confirmed according to the ventilation volume required for safe production. The initial air pressure of the local fan is P_f; the air pressure at the air outlet duct is represented by P_1; the air pressure at the inlet of the working face P_a can be obtained with consideration of the frictional resistance. Third, the air pressure at the outlet of the working face P_b can be calculated using pressure differences ΔP and the Equations previously shown. In addition, with friction resistance and air pressure variations, proper adjustment of the local fan and air window ensure an optimal pressure equalization ventilation mode. Taking 74104 high-temperature working face as an example, the optimized pressure equalization ventilation mode can effectively block the intrusion of goaf heat. Our results indicated that air temperature was reduced by 0.5–0.7 °C after the application of the optimized pressure equalization ventilation (Fig. 5).

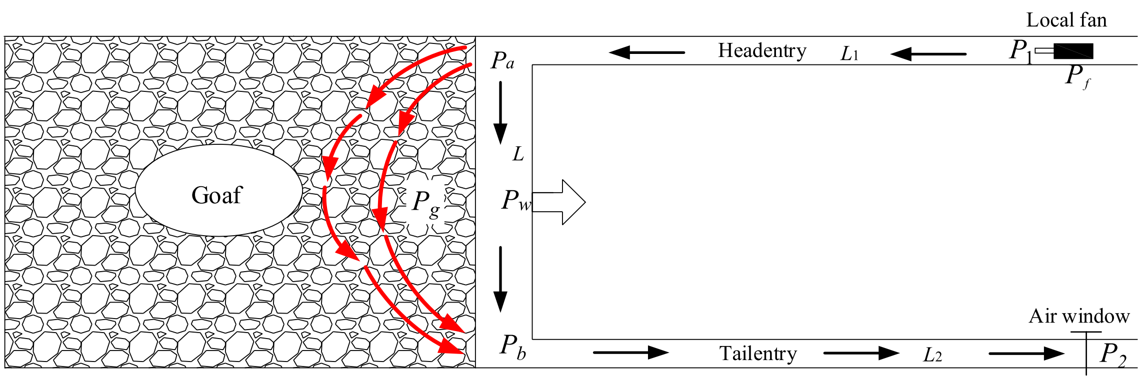

Fig. 4 Specific layout of pressure equalization ventilation system in high-temperature working face

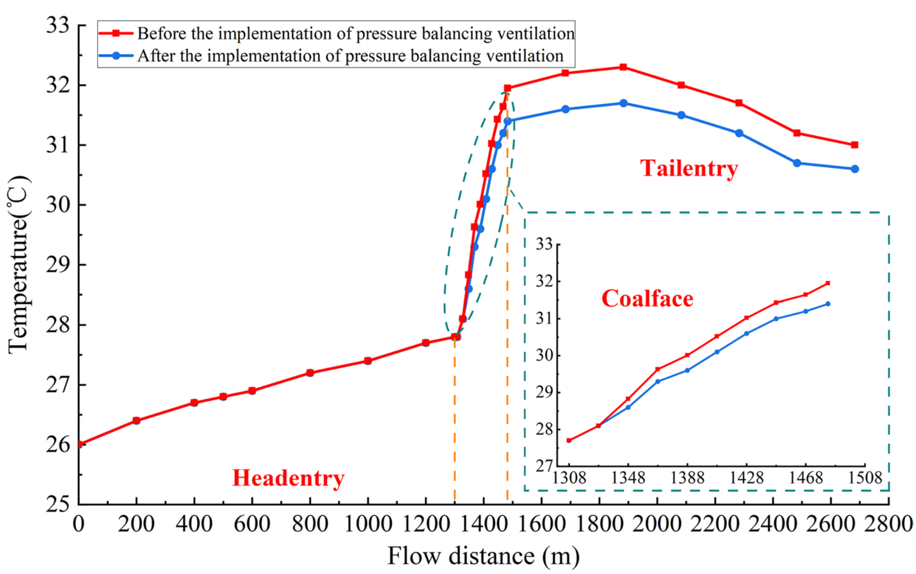

Fig. 5 Airflow temperature before and after the implementation of pressure equalization ventilation

4 Numerical simulation

4.1 Model setup

The working face is complex and contains multiple heat sources. Because of the influence of different heat sources such as high-temperature ribs and mechanical equipment, the temperature of the fresh airflow gradually increased. In this case, temperature measurements are inaccurate since the installation of the temperature and humidity sensor is difficult. Since the second step considers the design of the cooling system, it is important to determine the effect of multiple heat sources on airflow temperature. With this information, a more accurate system can be designed.

Figure 6 shows the airflow heat exchange model of the working face built using the COMSOL software. The model consisted of several cuboids with a length of 175 m, a width of 5 m, and a height of 4 m. The parameters were set up according to the distribution of the heat source in the working face. Thermal contribution of the personnel, coal cutter, and other heat sources all belong to absolute heat sources and are located in the same position. Thus, in the simulation, they can be considered as an integral heat source (Tu et al. 2021). The heat dissipation of coal and pillar rib transportation are averaged. In this case, temperature of coal transportation was 37 °C, the rib temperature 42 °C, and the convective heat transfer coefficient 6.565 W/(K m^2). The upper, lower, and left surfaces of the model were considered adiabatic walls. The heat dissipation of the goaf can be ignored after heat source barrier measures were implemented.

The temperature of the inlet airflow, air velocity, and rib temperature have an impact on the change of airflow temperature through the analysis of the heat exchange process of the working face. In order to analyze these effects, the control variate method was selected to set different initial parameters for the numerical simulation as illustrated in Table 1.

4.2 Variation of airflow temperature

Data in Fig. 7a indicate that the variation of airflow temperature in the working face can be divided into three stages. Between 0 and 90 m, the airflow temperature increases linearly with the increase in flow distance. Later, the increase trend changed between 90 and 110 m. This occurred because there is an absolute heat source concentration area where the

Table 1 Influencing factors of airflow temperature in working face

Group	Inlet airflow temperature (°C)	Air velocity (m/s)	Rib temperature (°C)
1	21	1.5	42
	24		
	28		
2	24	1.5	42
		2.0	
		2.5	
3	24	1.5	40
			42
			44

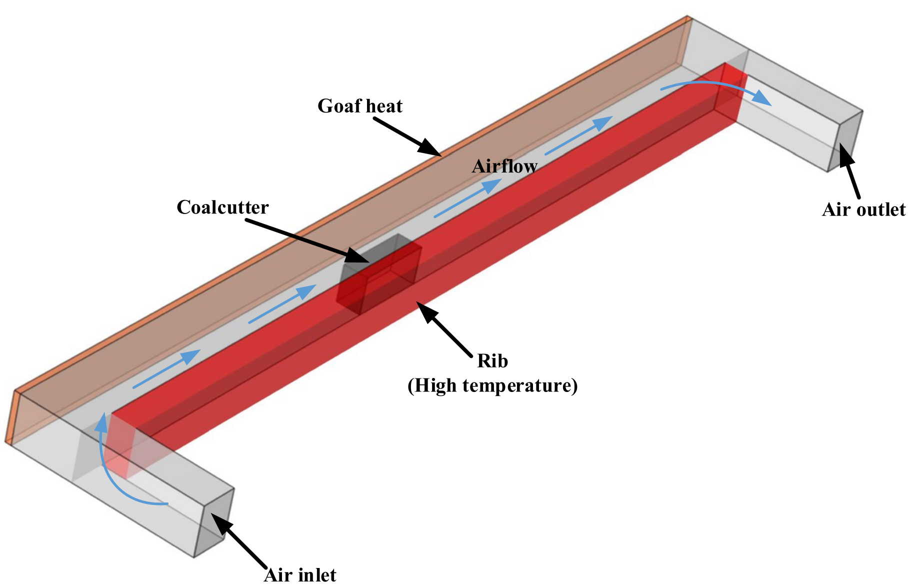

Fig. 6 Model of heat transfer between the airflow and the working face

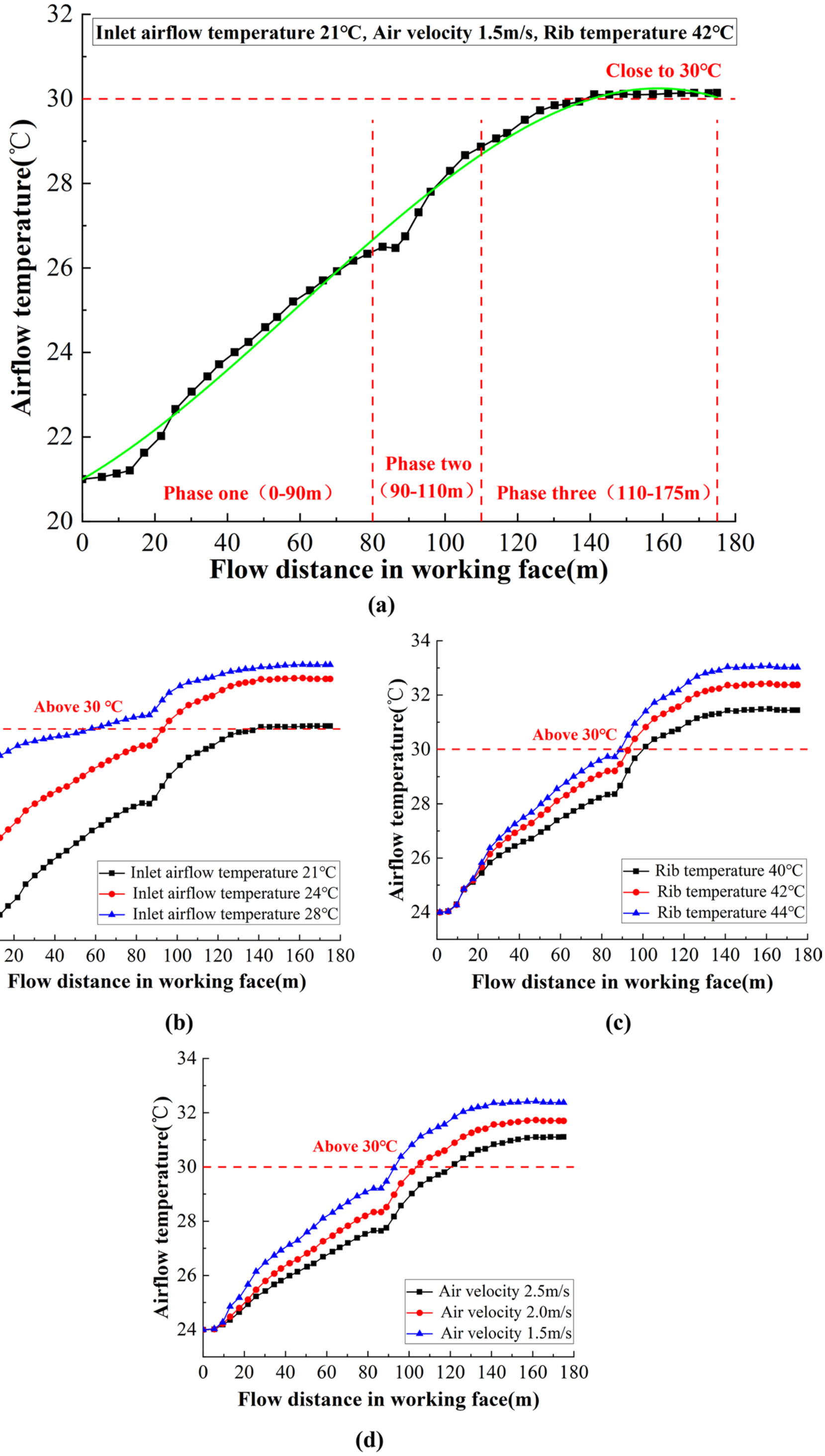

Fig. 7 **a** Unitive transformation law **b** Under different air inlet temperatures **c** Under different rib temperatures **d** Under different air velocities

heat increases significantly. Between 110 and 175 m, the airflow temperature still increases with the increase in flow distance; however, the increase amplitude diminished gradually until it approached to zero. At the final stage, the airflow temperature was close to 30 °C. When the temperature of the inlet airflow was 21 °C, that at the back of the working face slightly exceed 30 °C. This means that some cooling measures should be taken to ensure the safety of the mine as the inlet airflow temperature continues to rise.

Results in Fig. 7b–d indicate that the inlet airflow temperature, air velocity, and rib temperature affected airflow temperature. These data also showed that the higher the inlet airflow temperature, the higher the temperature of the returning airflow, and the smaller the amount of heat-exchanged between the airflow and the environment (Fig. 7b). Therefore, this method can be used to accurately monitor the temperature of the inlet airflow and determine if the working face requires to be cooled down. The results presented herein provide a model to estimate the temperature of the airflow and an intelligent strategy to control cooling devices.

Figure 7c indicates that, within the same flow distance, the higher the rib temperature, the larger the increase in airflow temperature, and the greater the value of the airflow temperature when stability is reached. In addition, the overall temperature of the airflow will not change in spite of variations in rib temperature. Moreover, a smaller difference in airflow temperatures were observed when rib temperatures were 44 °C and 42 °C, as compared to those of 42 °C and 40 °C. These data indicated that rib temperature was negatively correlated with Δt and the airflow temperature did not infinitely increased as rib temperatures also increased *(Δt is the difference of airflow temperatures corresponding to different rib temperatures)*.

Figure 7d indicates that the larger the air velocity, the smaller the increase in airflow temperature within the same flow distance, and the smaller the stable airflow temperature finally reached. This means that the environmental temperature of the working face can be reduced by increasing the amount of air. Our data indicate that the best way to cool down the high-temperature working face is by using a cooling equipment adapted with a supporting fan.

5 Results and discussion

5.1 Model of airflow temperature

In order to achieve a reasonable design of the cooling system and intelligent control of the cooling equipment, the accurate prediction of airflow temperature is required. Thus, in the present research, we obtained the airflow temperature prediction models of headentry, tailentry, and working face in different regions. We selected the airflow temperature prediction models of working face as example for detailed analysis.

The differential equation of heat balance in the working face was based on the law of conservation of energy. The amount of heat exchange between the heat source and airflow in the micro element is equal to the sensible heat of the airflow (manifested as the increase in airflow temperature) plus the latent heat of water vaporization (Qin and Xu 1998).

$$\mathrm{d}Q = M_{\mathrm{B}}\mathrm{d}i = M_{\mathrm{B}}c_{\mathrm{p}}\Delta t + M_{\mathrm{B}}\gamma\mathrm{d}x \tag{11}$$

where, $\mathrm{d}Q$ indicates the amount of heat exchange between the heat source and airflow in micro element of the working face; M_{B} is the air mass flow rate; c_{p} corresponds to the specific heat at constant pressure; γ is the latent heat of vaporization; x indicates moisture content; i is the enthalpy of incoming airflow; and Δt is the increment of airflow.

Considering the heat sources in the working face, the heat transferred by the thermal environment to the airflow contained in the micro-element of the working face is determined using Eq. (12):

$$\mathrm{d}Q = K_{\tau}U\left(t_{\mathrm{w}} - t\right)\mathrm{d}y + \frac{Q_{\mathrm{s}} + Q_{\mathrm{c}} + Q_{\mathrm{h}} + Q_{\mathrm{r}} + Q_{\mathrm{z}}}{L}\mathrm{d}y \tag{12}$$

Rib and coal transportation are both heat sources, and the heat transferred from coal transportation to airflow is calculated using Eq. (13) (Zhu et al. 2020):

$$Q_{\mathrm{s}} = G_{\mathrm{s}}c_{\mathrm{s}}\Delta t = 0.0024L^{0.8}G_{\mathrm{s}}c_{\mathrm{s}}(t_{\mathrm{avg}} - t_{\mathrm{fh}}) \tag{13}$$

There is an approximate linear relationship between moisture content of airflow and airflow temperature at standard atmospheric pressure (Danko et al. 2020).

$$\begin{aligned} x &= \left(\varphi_1 + \frac{\Delta\varphi}{L}y\right)At + \left(\varphi_1 + \frac{\Delta\varphi}{L}y\right)D \\ &\Rightarrow \mathrm{d}x = \left(\varphi_1 + \frac{\Delta\varphi}{L}y\right)A\mathrm{d}t + \frac{\Delta\varphi}{L}(At + D)\mathrm{d}y \end{aligned} \tag{14}$$

Solving the simultaneous Eqs. (11), (12), (13), (14) and after the simplification process, we obtained Eq. (15):

$$\begin{cases} E = 1 + \dfrac{A\gamma}{c_{\mathrm{p}}}\varphi_2 \\ F = \dfrac{A\gamma\Delta\varphi}{c_{\mathrm{p}}L} \\ \eta = 0.0024L^{0.8}G_{\mathrm{s}}c_{\mathrm{s}} \\ \Sigma Q_{\mathrm{M}} = Q_{\mathrm{c}} + Q_{\mathrm{h}} + Q_{\mathrm{r}} + Q_{\mathrm{z}} \end{cases} \tag{15}$$

The nonhomogeneous first order linear differential equation with only t and y as the variable parameters was obtained as shown in Eq. (16):

$$\frac{\mathrm{d}t}{\mathrm{d}y} + \frac{\left(\frac{\eta\sigma}{LM_{\mathrm{B}}c_{\mathrm{p}}} + \frac{K_{\tau}U}{M_{\mathrm{B}}c_{\mathrm{p}}} + \frac{\gamma\Delta\varphi A}{Lc_{\mathrm{p}}}\right)}{E + Fy}t = \frac{\frac{K_{\tau}Ut_{\mathrm{w}}}{M_{\mathrm{B}}c_{\mathrm{p}}} + \frac{\eta t_{\mathrm{avg}}}{LM_{\mathrm{B}}c_{\mathrm{p}}} + \frac{\Sigma Q_{\mathrm{M}}}{LM_{\mathrm{B}}c_{\mathrm{p}}} - \frac{\Delta\varphi\gamma D}{Lc_{\mathrm{p}}}}{E + Fy} \tag{16}$$

The relationship between the working face airflow temperature t and the working face airflow distance y is obtained by solving the previous differential equation, as seen in Eq. (17).

$$t = \frac{K_\tau U t_w L + \eta t_{avg} + \Sigma Q_M - M_B \Delta\varphi\gamma D}{K_\tau U L + \eta\sigma + M_B \Delta\varphi\gamma A} + \left[\left(t1 - \frac{K_\tau U t_w L + \eta t_{avg} + \Sigma Q_M - M_B \Delta\varphi\gamma D}{K_\tau U L + \eta\sigma + M_B \Delta\varphi\gamma A}\right) \times E^{\frac{K_\tau UL + \eta\sigma + M_B \Delta\varphi\gamma A}{M_B \Delta\varphi\gamma A}}\right] \times (E + Fy)^{-\frac{K_\tau UL + \eta\sigma + M_B \Delta\varphi\gamma A}{M_B \Delta\varphi\gamma A}} \tag{17}$$

where, t_w is the rib temperature; t_{avg} is the average temperature during coal transportation; t_{fh} indicates the wet bulb temperature of airflow, $t_{fh} = \sigma t$, σ equals to 0.904; t_1 indicates the airflow temperature in working face inlet; G_s is the coal mass flow rate; c_s corresponds to the specific heat of coal; K_τ is the unstable heat transfer coefficient; U represents the perimeter of the working face section; L is the length of the working face; φ_1 is the relative humidity of inlet airflow; $\Delta\varphi$ is the difference between the relative humidity of airflow at the inlet and that at the outlet; and $\sum Q_M$ is the sum of the absolute heat exothermic quantity in the working face. The airflow temperature at each point of the working face can be solved by using Eq. (17).

The airflow temperature prediction model of headentry can be obtained in a similar way, as seen in Eq. (18). Herein, t_0 represents the airflow temperature in headentry inlet and $\sum Q_{M1}$ represents the sum of the absolute heat exothermic quantity in the headentry.

$$t = \frac{K_{\tau 1} U_1 t_{w1} L_1 + \Sigma Q_{M1} - M_B \Delta\varphi\gamma D}{K_{\tau 1} U_1 L_1 + M_B \Delta\varphi\gamma A} + \left[\left(t_0 - \frac{K_{\tau 1} U_1 t_{w1} L_1 + \Sigma Q_{M1} - M_B \Delta\varphi\gamma D}{K_{\tau 1} U_1 L_1 + M_B \Delta\varphi\gamma A}\right) \times E^{\frac{K_{\tau 1} U_1 L_1 + M_B \Delta\varphi\gamma A}{M_B \Delta\varphi\gamma A}}\right] \times (E + Fy)^{-\frac{K_{\tau 1} U_1 L_1 + M_B \Delta\varphi\gamma A}{M_B \Delta\varphi\gamma A}} \tag{18}$$

The model to predict airflow temperature at the tailentry is presented in Eq. (19). In this case, t_2 represents the airflow temperature at inlet tailentry and $\sum Q_{M2}$ represents the sum of the absolute heat of the exothermic process at the tailentry.

$$t = \frac{\eta t_{avg} + \Sigma Q_{M2} - M_B \Delta\varphi\gamma D}{\eta\sigma + M_B \Delta\varphi\gamma A} + \left[\left(t_2 - \frac{\eta t_{avg} + \Sigma Q_{M2} - M_B \Delta\varphi\gamma D}{\eta\sigma + M_B \Delta\varphi\gamma A}\right) \times E^{\frac{\eta\sigma + M_B \Delta\varphi\gamma A}{M_B \Delta\varphi\gamma A}}\right] \times (E + Fy)^{-\frac{\eta\sigma + M_B \Delta\varphi\gamma A}{M_B \Delta\varphi\gamma A}} \tag{19}$$

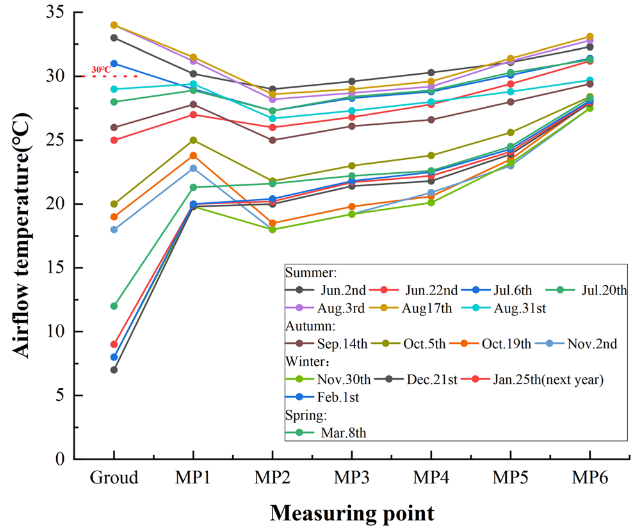

Fig. 8 Airflow temperatures at different measuring points in different periods

5.2 Accuracy of prediction model

In order to ensure that the model to predict airflow temperature can be applied to the whole production cycle of the mine and that it is able to resemble underground temperature changes caused by seasonal variations as well as thermal flywheel effect and others, we analyzed the measured data and identified the dominant factors affecting underground temperature changes. Based on this, the measured data of airflow temperature with certain seasonal representativeness were selected for model verification. The measured wind temperature at each measuring point in different periods of 74104 working face are shown in Fig. 8.

Figure 8 shows that the seasonal variation will have a significant impact on temperature levels in underground environments. During the summer, the underground also faces high temperatures and heat damages, especially from June to August. Even after cooling, the wind temperature of the 74104 working face will still exceed 30 °C, which requires secondary cooling measures. In autumn, from September to mid-November, high temperature periods lead to thermal damage events; however, the overall climate of the mine is good. In winter, from late November to mid and late February, safe mining can be ensured without refrigeration and cooling measures. Spring runs from March to May. In this case, the situation is similar to autumn. Therefore, selected data should include that corresponding to summer, autumn (or spring), and winter.

As shown in Fig. 8, the critical value of the ground temperature is 30 °C. When temperature is higher than 30 °C, the airflow temperature gradually decreases in the process of underground flow. On the contrary, the airflow temperature increases gradually, which is caused by the thermal flywheel effect (Scalise et al. 2021; Roghanchi and Kocsis 2019). This effect has a certain influence on the arrangement of ventilation and cooling system. Therefore, it is necessary to consider this point when selecting reasonable measured wind temperature data. In addition, the ground weather changes and diurnal changes will also have a certain impact on the selection of measured data and the verification of the prediction model. Nevertheless, the changes can be included in the temperature range of the four seasons, and not considered as an independent factor in the selection of measured data.

Based on this, we divided the whole production cycle of working face into four representative periods: above 30 °C (mainly in summer), 20–30 °C (summer and part of spring and autumn), 10–20 °C (mainly in spring and autumn), and below 10 °C (mainly in winter). Therefore, we selected the measured air flow temperature data on June 22nd (summer), August 3rd (summer), October 19th (autumn) and November 30th (winter) to verify the wind temperature prediction model (Tables 2 and 3). In addition, June 2nd was selected as the starting time of data recording, and this date belongs to the period above 30 °C. Wind temperature recorded on June 2nd was considered the preliminary reference basis for the cooling and cooling system layout of the 74104 working face, which provide safe cooling conditions of 74104 working face. The optimal cooling system layout scheme needs to further consider the cooling demand in the ultra-high temperature period in summer. The cooling system layout method will be analyzed and introduced in detail in Section 4.4.

Multiple groups of calculated data and measured data were plotted using Origin. The results are shown in Fig. 9.

The results indicated that the model to predict airflow temperature can be used with a certain margin of error. The cooling capacity of the working face can be obtained through the temperature airflow prediction results, which provides a theoretical basis for the formulation of intelligent control strategy of cooling equipment.

Table 2 Airflow temperature in the intake roadway of 74104 working face

Flow distance (m)	June 22nd	August 3rd	October 19th	November 30th
0	26.0	28.2	18.5	18.0
200	26.4	28.5	19.1	18.5
400	26.7	28.6	19.6	19.0
500	26.8	28.5	19.8	19.2
600	26.9	28.7	20.0	19.5
800	27.2	28.8	20.5	19.9
1000	27.4	29.0		
1200	27.7			
1300	27.8			

Table 3 Airflow temperature of the 74104 working face

Flow distance (m)	June 22nd	August 3rd	October 19th	November 30th
0	27.7	29.2	20.6	20.1
20	28.1	29.6	21.7	21.2
40	28.6	30.2	22.5	22.0
60	29.3	30.7	23.5	23.2
80	29.6	31.2	24.4	24.0
100	30.1	31.7	25.3	24.8
120	30.6	32.3	26.0	25.7
140	31.0	32.6	26.7	26.5
160	31.4	32.7	27.4	27.5
175	31.4	32.8	28.0	27.8

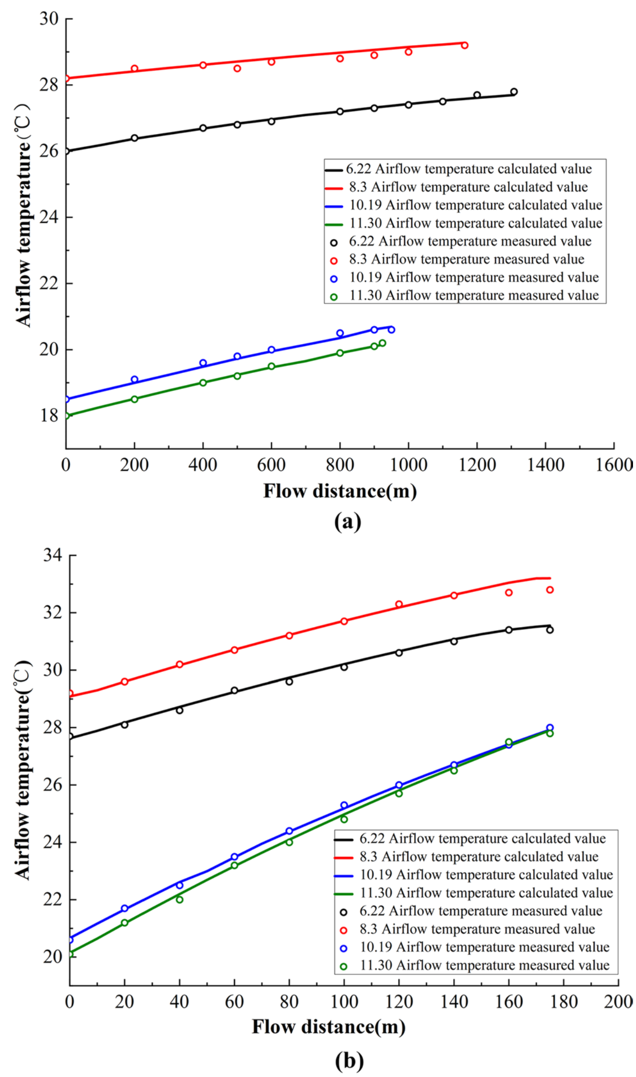

Fig. 9 **a** Comparison between the measured and calculated airflow temperature in headentry **b** Comparison between the measured and calculated airflow temperature in the working face

5.3 Model applicability analysis

After verifying the accuracy of the airflow temperature prediction model, it is necessary to analyze its applicability and determine its potential limitations. The model was determined considering ventilation parameters, roadway layout parameters, and thermal physical parameters of the heat source. Therefore, when the roadway layout or ventilation mode of the working face changes, the matching airflow temperature prediction model can be established by adjusting relevant parameters. Unfortunately, the current model is more applicable to underground mining because it was built considering the ventilation of shafts and roadways. Since the previous research and data measurement were performed for coal mining conditions, it is impossible to clarify the applicability of the model and methods for non-coal mining cases. However, further research will be performed in order to provide a reference value for the establishment of the airflow temperature model of non-coal mining working faces in underground mining.

5.4 Industrial application

In the present research, an energy-saving and efficient cooling scheme for high-temperature working faces in deep mines was proposed. For this purpose, the previous theoretical analysis and field measurements were considered. The system included the selection of the initial position of the cooling equipment and the intelligent control strategy by considering working face distance and seasonal airflow temperature variations. Field test of cooling scheme was carried out relying on the actual engineering background of 74104 high-temperature working face.

Zhangshuanglou Coal Mine can be divided into the east wing and the west wing mining area. Each wing is equipped with a set of German Pegasus KM2000 underground centralized chiller and a KM1000 unit in the −750 m main refrigeration chamber, with a total refrigeration capacity of 3000 kW. The 74104 working face is located in the west wing. According to the mining and excavation replacement plan of the mine, the cooling system of the west wing mine needs to conduct refrigeration and cooling operations on the 74104 working face, 94102 heading face and 94602 heading face at the same time. Therefore, the total cooling capacity that can supply the 74104 working face is 1000 kW. The working face started mining activities on June 1st, and the air flow temperature at the inlet of the inlet tunnel of the working face was 29 °C on June 2nd. To ensure that working face production is carried out in a safe environment, the relationship between the cooling capacity required for the working face and the layout position were determined. Results are shown in Table 4.

According to data presented in Table 4 (characters in bold), when the cooling equipment was placed 1000 m away from the airflow inlet of the working face, the cooling capacity was 970 kW, which is smaller than the 1000 kW required for cooling the working face. In addition, the working face is not able to reach the cooling demands as the distance increases. Therefore, the cooling equipment is initially placed in the refrigeration chamber within 1000 m from the inlet of the working face. Also, the cooling equipment layout needs to consider whether it can comply with the cooling demand of the working face during the high temperature period. The maximum airflow temperature was found from the recorded data for further analysis. The measured airflow before cooling was 30.6 °C (The hottest time of the year) and the advance distance was 210 m on August 10th. Then, the airflow temperature after cooling can be calculated according to the cooling capacity of 1000 kW, and finally the change of return airflow temperature of working face under different layout positions are obtained, as seen in Table 5.

Table 4 Cooling requirements at different positions

Distance from working face (m)	Airflow temperature after cooling (°C)	Airflow temperature before cooling (°C)	Cooling requirement (kW)
1374	18.97	29	1060.1
1200	19.29	29	1033.2
1100	19.62	29	1006.4
1000	**19.99**	**29**	**970.8**
900	20.38	29	936.9
800	20.69	29	908.5
700	20.98	29	881.6
600	21.29	29	853.2
500	21.60	29	824.6
400	21.82	29	805.7

Table 5 (Bold lines) indicates that the returning airflow temperature is almost close to the critical temperature of 30 °C when the cooling equipment is 590 m away from the inlet of the working face. In conclusion, with the working face advance distance of 210 m, the cooling equipment ought to be arranged in the refrigeration chamber within 800 m from the inlet of the working face at the beginning of mining activities. This set up will provide the proper cooling conditions during the whole mining cycle, without the need of frequently "moving" the equipment. The optimal effect can be achieved with this scheme.

In order to achieve safe conditions, energy conservation, and high efficiency, it is necessary to formulate an intelligent strategy for controlling the cooling equipment by considering the initial position of cooling equipment. The cooling capacity is dynamically adjusted with seasonal variations and advancement of the working face. Table 6 presents the return airflow temperature under different cooling capacities in late September. The average airflow temperature before cooling is 25 °C and the advance distance is 345 m at this moment.

Table 5 Airflow temperature of headentry and tailentry under different layouts

Distance from working face (m)	Airflow temperature before cooling (°C)	Airflow temperature after cooling (°C)	Inlet airflow temperature (°C)	Return airflow temperature (°C)
190	30.6	22	22.54	29.32
290	30.6	22	22.81	29.48
390	30.6	22	23.07	29.65
490	30.6	22	23.32	29.82
590	**30.6**	**22**	**23.61**	**29.98**
690	30.6	22	23.89	30.19
790	30.6	22	24.14	30.38
890	30.6	22	24.39	30.54
990	30.6	22	24.62	30.70
1090	30.6	22	24.81	30.82

Table 6 Return airflow temperature under different cooling capacities

Airflow temperature before cooling (°C)	Cooling capacity (kW)	Airflow temperature after cooling (°C)	Inlet airflow temperature (°C)	Return airflow temperature (°C)
25	100	24.0	24.98	30.93
25	200	23.3	24.37	30.53
25	**265**	**22.4**	**23.56**	**29.99**
25	300	22.0	23.23	29.78
25	400	20.9	22.27	29.15
25	500	19.7	21.22	28.47
25	600	18.6	20.25	27.83
25	700	17.3	19.12	27.09

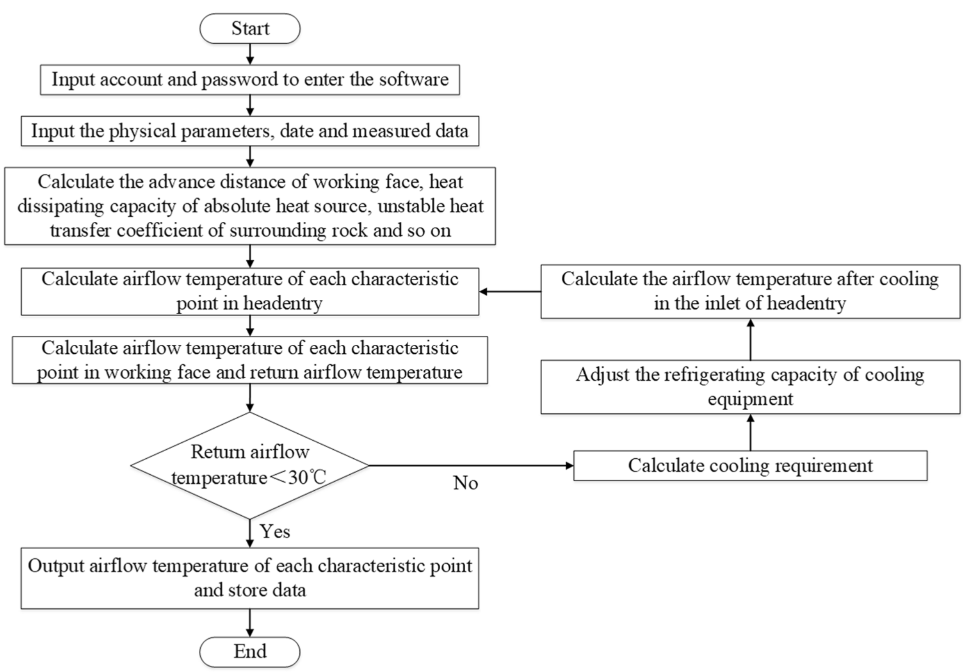

Fig. 10 Intelligent control strategy of cooling equipment

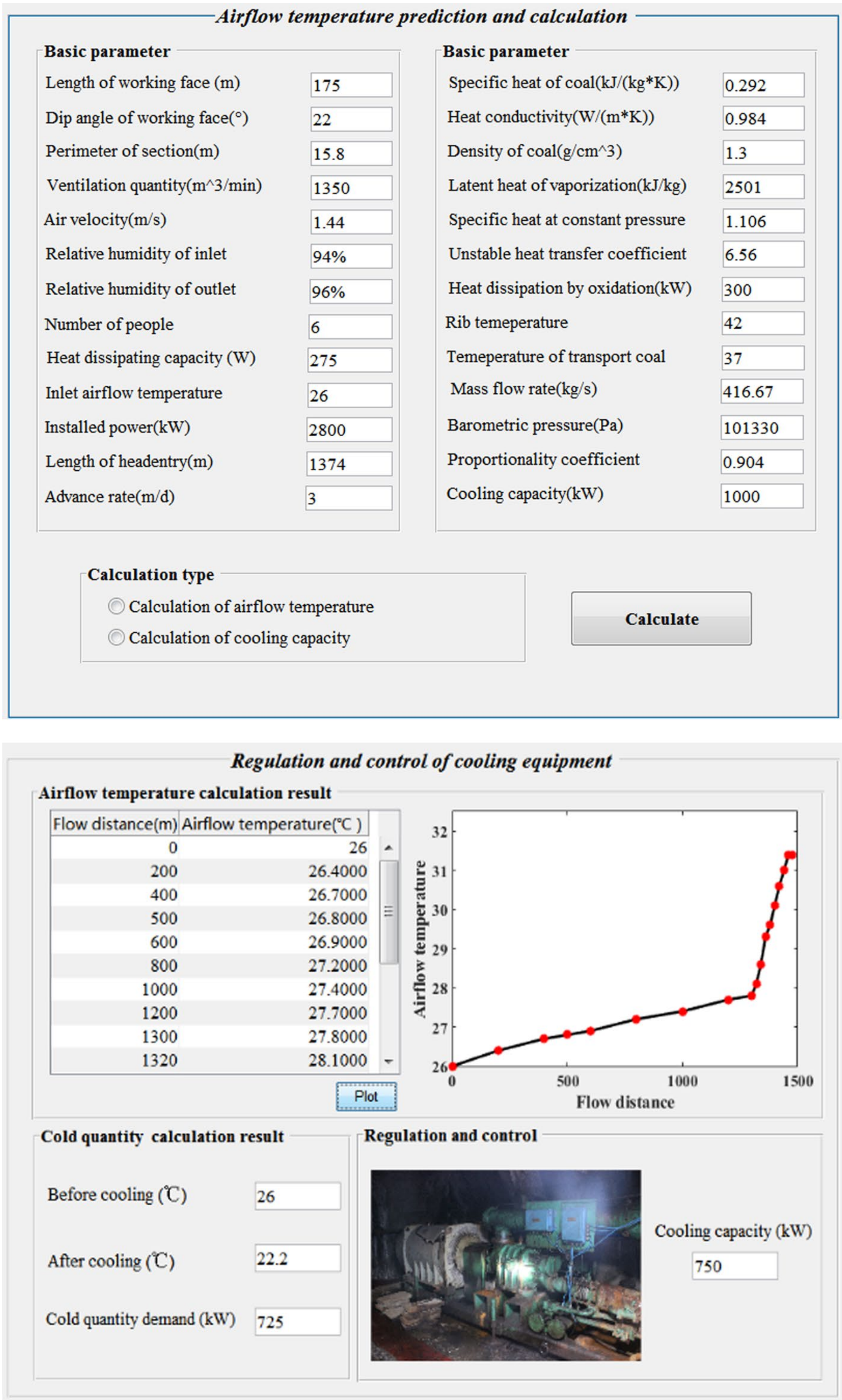

Fig. 11 Software operation interface

Table 6 (Bold lines) indicates the cooling capacity of 265 kW can meet the cooling demand of the working face in late September, the return airflow temperature is lower than the critical temperature of 30 ℃ under this condition. The airflow temperature at inlet of headentry and the flow distance decreased gradually with seasonal variations and advancement of the working face. As Table 6 shows, safety mining can be performed without opening the cooling

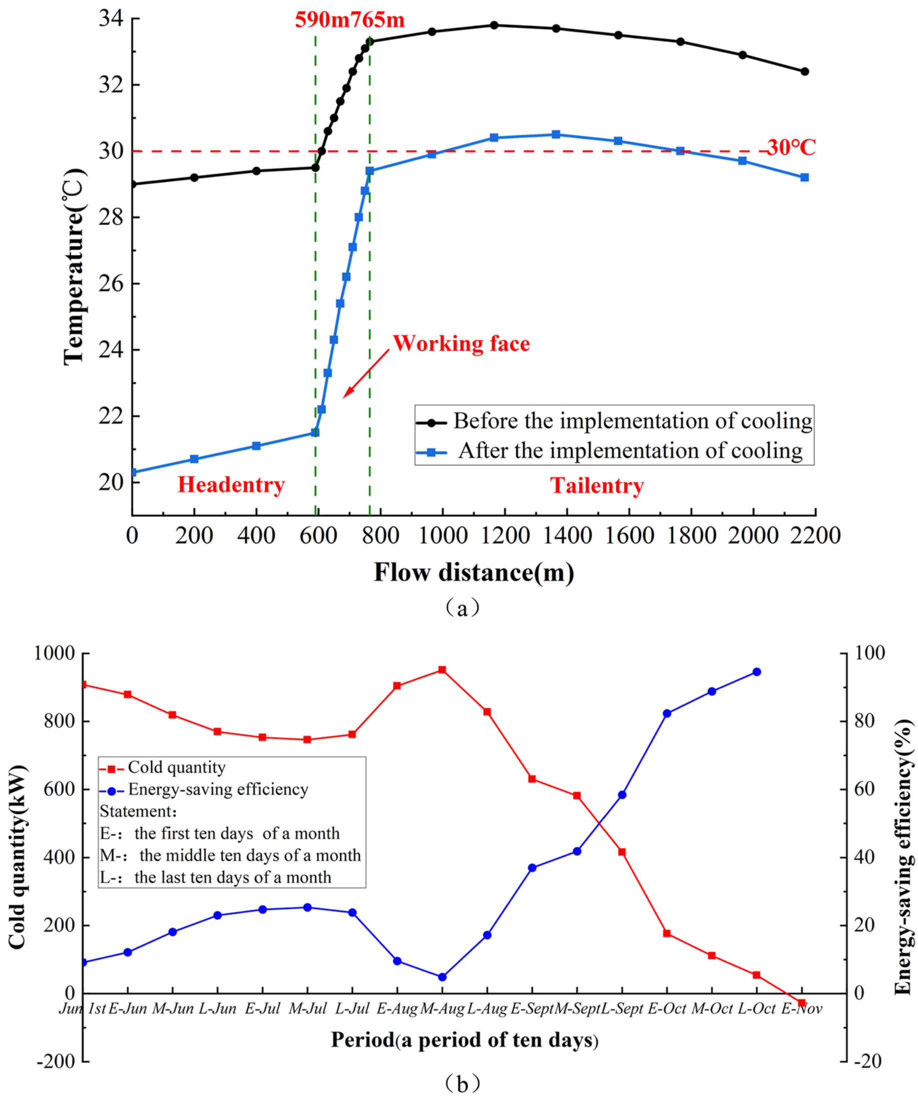

Fig. 12 **a** Airflow temperature before and after the implementation **b** Cold quantity demand and energy-saving efficiency in the full mining cycle

equipment when the airflow temperature is less than 22 °C. Thus, the intelligent control strategy of the cooling equipment can be summarized. “A period of ten days” was taken as a time to adjust the cooling capacity and appropriately reduce the period of regulation in the active phase of airflow temperature variation. Besides, an intelligent control software with intelligent control strategy was developed to facilitate field application, as seen in Figs. 10 and 11.

The airflow thermal parameter of the working face was measured after the cooling scheme and intelligent control strategy were applied to the 74104 working face. Figure 12a presents the change of airflow temperature before and after cooling. In addition, the average cooling capacity was determined on a period of ten days rotation, and the saving energy consumption of refrigeration after the application of the new cooling scheme was calculated, as seen in Fig. 12b.

Figure 12a indicates that the thermal hazard threat has been significantly reduced, the return airflow temperature can be maintained at 29.4 °C, which is 4 °C lower than that before the implementation of cooling scheme. Figure 12b indicates that the safety mining can be guaranteed without any cooling measures after November. In addition, a 10% in energy saving efficiency can be reached during the high temperature period, and more than 50% in low temperature period after the application of the new intelligent cooling scheme. The new cooling scheme can dramatically reduce the waste of power energy. This complies with the requirements for safe mining, high efficiency, and green and energy conservation.

6 Conclusions

In the present research, we selected the 74104 high-temperature working face as engineering background. After combining theoretical analysis, numerical simulation, and field investigation, we obtained the following conclusions.

(1) Given the characteristics of complex heat sources, scattered heat source locations, and severe regional heat damage threats in high-temperature working faces, we proposed a combined scheme for heat hazard prevention and control described as "heat source barrier + cooling equipment". In addition, the present research focused on the heat barrier method of pressure equalization ventilation and dynamic control strategy of the cooling equipment.

(2) The numerical simulation method was used to obtain the variation rule of airflow temperature affected by multiple heat sources. We proposed models to predict airflow temperature of headentry, tailentry, and working face by considering the variation rule of airflow temperature. Then, and automatic control software was designed for the 74104 high-temperature working face. The cooling equipment was arranged in the refrigeration chamber within 800 m from the inlet of the working face and the period of regulation was “a period of ten days”.

(3) After the application of the proposed composite cooling scheme, the ambient temperature was always below 30 °C, and the energy saving efficiency reached 10% during the high-temperature period and more than 50% in the low temperature period. The scheme proposed herein properly complies with the requirements of safety, high efficiency, and green and energy conservation. In addition, it provides reference for similar heat harm control in high-temperature working faces.

Acknowledgements This study was supported by the National Natural Science Foundation of China (51874281), the Graduate Innovation Program of China University of Mining and Technology (2022WLKXJ006) and the Postgraduate Research & Practice Innovation Program of Jiangsu Province (KYCX22_2612).

Author contributions All authors contributed to the study conception and design. Conceptualization were performed by Hongbin Zhao and Xun Liu. Methodology were performed by Shihao Tu. Data curation was performed by Jieyang Ma and Long Tang. The first draft of the manuscript was written by Hongbin Zhao. All authors have read and agreed to the published version of the manuscript.

Declarations

Competing interests The authors declare that they have no competing interests.

References

Bluhm S, Moreby R, von Glehn F, Pascoe C (2014) Life-of-mine ventilation and refrigeration planning for resolution copper mine. J South Afr Inst Min Metall 114(6):497–503

Brake R, Fulker B (2000) The ventilation and refrigeration design for Australia's deepest and hottest underground operation—the enterprise mine

Buys JL, Kleingeld M, Cilliers C (2015) Optimizing the refrigeration and cooling system of a platinum mine. In: Proceedings of the 13th conference on the industrial and commercial use of energy, pp 36–43

Chang Z, Ji J, Wang K, Ni L, Li N (2021) Heat absorption control equation and its application research of cool-wall cooling system in mines. J Cent South Univ 15:1–25

Danko G, Bahrami D, Stewart C (2020) Applications and verification of a computational energy dynamics model for mine climate simulations. Int J Min Sci Technol 30:483–493

Du Plessis GE, Liebenberg L, Mathews E (2013) Case study: the effects of a variable flow energy saving strategy on a deep-mine cooling system. Appl Therm Eng 102(SI):700–709

Guo P, He M, Zheng L, Zhang N (2017) Research and development of HEMS cooling system and heat-harm control in deep mine. Appl Therm Eng 7:1353–1361

Hardcastle SG, Kocsis CK (2004) The ventilation challenge. CIM Bull 97(1080):51–57

Jayasuriya J, Moser I, de Mel R (2022) An automated water dispensing system for controlling fires in coal yards. Int J Coal Sci Technol 9(1):23. https://doi.org/10.1007/s40789-022-00488-y

Kuyuk AF, Ghoreishi-Madiseh SA, Hassani FP (2019) Performance and economic assessment of large-scale deep-lake cooling systems: a Canadian example. Energy 158:43–48

Liu L, Zhang J (2017) Thermal insulation composite material for governance of underground thermal hazard and its application. J Shandong Univ Sci Technol 36:46–53

Liu H, Wang J, Zhao J, Zhu M (2018) Critical technical problems of deep mining and preliminary solutions. Min Res Dev 38:1–5

Lolon SA, Brune JF, Bogin GE, Grubb JW (2017) Computational fluid dynamics simulation on the longwall gob breathing. Int J Min Sci Technol 27:185–189

Qin Y, Xu G (1998) Prediction of air temperature in heading face and calculation of cooling amount. J China Coal Soc 23:611–615

Ray SK, Singh RP (2007) Recent developments and practices to control fire in underground coal mines. Fire Technol 43:285–300

Roghanchi P, Kocsis KC (2019) Quantifying the thermal damping effect in underground vertical shafts using the nonlinear autoregressive with external input (NARX) algorithm. Int J Min Sci Technol 29(2):255–262

Scalise KA, Teixeira MB, Kocsis KC (2021) Managing heat in underground mines: the importance of incorporating the

thermal flywheel effect into climatic modeling. Min Metall Explor 38(1):575–579
Tamminen J, Ahonen T, Ahola J, Hammo S (2016) Fan pressure-based testing, adjusting, and balancing of a ventilation system. Energ Eff 9:425–433
Tu R, Huang L, Jin A, Zhang M, Hai X (2021) Characteristic studies of heat sources and performance analysis of free-cooling assisted air conditioning and ventilation systems for working faces of mineral mines. Build Simul 14:1725–1736
Wang H, Zhou Q (2020) Finite element analysis of surrounding rock with a thermal insulation layer in a deep mine. Math Probl Eng 2020:1–11
Wang J, Wan Z, Zhang H, Wu D, Zhang Y, Wang Y, Xiong L, Wang G (2020) Application of thermal insulation gunite material to the high geo-temperature roadway. Adv Civ Eng 2020:1–12
Wu F, Lou Y, Chang X (2019) Coupling simulation model between mine ventilation network and gob flow field. J South Afr Inst Min Metall 119:783–792
Xue D, Hu X, Cheng W, Wu M, Shao Z, Li Y, Zhao Y, Zhang K (2020) Carbon dioxide sealing-based inhibition of coal spontaneous combustion: a temperature-sensitive micro-encapsulated fire-retardant foamed gel. Fuel 266:1170360
Yao W (2018) The status and progress of the research on thermal environment of deep mine in China. Min Saf Environ Prot 45:107–111
Yoshida A, Okawa T, Ebina W, Naito H (2015) Experimental and numerical investigation of flame speed retardation by water mist. Combust Flame 162:1772–1777
Zhai X, Xu Y, Yu Z (2019) Design and performance simulation of a novel liquid CO_2 cycle refrigeration system for heat hazard control in coal mines. J Therm Sci 28:585–595
Zhang C, Tu S, Zhao Y (2019) Compaction characteristics of the caving zone in a long-wall goaf: a review. Environ Earth Sci 78:1–20
Zhang W, Wang T, Zhang D, Tang J, Xu P, Duan X (2020) A comprehensive set of cooling measures for the overall control and reduction of high temperature-induced thermal damage in oversize deep mines: a case study. Sustainability 12:2489–2493
Zhu S, Cheng J, Wang Z, Borowski M (2020) Physical simulation experiment of factors affecting temperature field of heat adjustment circle in rock surrounding mine roadway. Energy Source Part A Recov Util Environ Eff 2020:1–18
Zou S, Li K, Zhang D, Cao Y, Ding Y (2016) On the air-partition foe cooling with the heat insulated plate. J Saf Environ 16:99–102